Tectonophysics 931 (2026) 231206

Contents lists available at ScienceDirect

Tectonophysics

journal homepage: www.elsevier.com/locate/tecto

Pn-wave attenuation tomography beneath the Alaskan mainland: Implications for volcanism genesis and toroidal mantle flow

Geng Yang [a], Lian-Feng Zhao [b,c,*], Xiao-Bi Xie [d], Yingjie Yang [a,*], Zhen-Xing Yao [b]

[a] Department of Earth and Space Sciences, Southern University of Science and Technology, Shenzhen, China
[b] Key Laboratory of Planetary Science and Frontier Technology, Institute of Geology and Geophysics, Chinese Academy of Sciences, Beijing, China
[c] Heilongjiang Mohe Observatory of Geophysics, Institute of Geology and Geophysics, Chinese Academy of Sciences, Beijing, China
[d] Institute of Geophysics and Planetary Physics, University of California at Santa Cruz, CA95064, USA

ARTICLE INFO

Keywords:
Pn-wave attenuation tomography
Alaskan mainland
Yakutat microplate
Denali volcanic gap
Intraplate volcano
Toroidal mantle flow

ABSTRACT

The Alaskan mainland lies above the subducting Pacific, Yakutat, and Wrangell slabs. Volcanoes of different types are primarily distributed in western and south-central Alaska. However, the formation mechanisms of these arc and intraplate volcanoes, as well as the Denali volcanic gap (DVG), remain unclear and debated. We developed a high-resolution Pn-wave attenuation tomographic model to investigate the thermal structure of the uppermost mantle beneath Alaska. Strong attenuation anomalies in western Alaska reveal two high-temperature regions beneath the intraplate volcanoes. Their spatial correspondence with the stagnant Pacific plate suggests that intraplate volcanism may be driven by mantle upwelling associated with the “big mantle wedge” structure. In south-central Alaska, the weak attenuation features observed beneath the DVG indicate that flat-slab subduction of the Yakutat slab has cooled the mantle wedge and crust, inhibiting the generation of partial melts and resulting in the absence of volcanism. A toroidal melting zone surrounding the Yakutat plate is also identified in the uppermost mantle, aligning closely with the inferred location of toroidal mantle flow. The molten materials transported by this toroidal mantle flow may supply magma to the Wrangell volcanic field and the Buzzard Creek–Jumbo Dome volcanoes.

1. Introduction

The Alaskan mainland, overlying the subducting Pacific, Yakutat, and Wrangell plates, serves as an ideal region for studying subduction dynamics and volcanism (Figs. 1a-1b). Despite extensive research over the past decade, the mechanism responsible for the formation of intraplate and arc volcanoes in Alaska remains unclear. The Yakutat oceanic microplate originated from the Kula–Farallon spreading ridge around 50 Ma, migrated northward along the Queen Charlotte–Fairweather fault system (Plafker et al., 1994), and collided with the North American continent during the Oligocene–Miocene, undergoing flat-slab subduction (Eberhart-Phillips et al., 2006). Around the Yakutat plate, arc volcanism is absent from $\sim 152^{\circ} W$ and resumes in the Buzzard Creek–Jumbo Dome volcanic region (BJV) at $\sim 147^{\circ} W$, and this zone is known as the Denali volcanic gap (DVG). The formation of the DVG has been consistently attributed to the flat subduction of the Yakutat plate (e.g., Christeson et al., 2010; Chuang et al., 2017). The high-velocity upper mantle beneath the DVG further indicates that molten magmatic materials do not exist in this region (Jiang et al., 2018; Ward and Lin, 2018; Yang and Gao, 2020). However, some tomographic studies have identified several low-velocity anomalies in the mantle wedge and crust beneath the DVG (Feng and Ritzwoller, 2019; Gou et al., 2019; Martin-Short et al., 2018; Rabade et al., 2023). These observations are difficult to reconcile with the absence of surface volcanism.

East of the Yakutat plate, the Wrangell slab exhibits minimal Wadati–Benioff zone (WBZ) seismicity (Gou et al., 2019; Jiang et al., 2018) and is overlain by the Wrangell volcanic field (WVF). The relationship between the magmatic source of the WVF and the subducting slabs remains controversial. Several hypotheses have been proposed: (1) Melting of the Yakutat slab edge could explain the presence of adakites along the south-facing edge of the WVF (Preece and Hart, 2004). (2) A slab tear or gap may provide a channel supplying magma to the WVF (Gou et al., 2019; Mann et al., 2022). (3) The subduction of the Wrangell

---

* Corresponding authors at: Key Laboratory of Planetary Science and Frontier Technology, Institute of Geology and Geophysics, Chinese Academy of Sciences, 19 Beituchengxilu, Chaoyang District, Beijing 100029, China.

E-mail addresses: zhaolf@mail.iggcas.ac.cn (L.-F. Zhao), yangyj@sustech.edu.cn (Y. Yang).

https://doi.org/10.1016/j.tecto.2026.231206
Received 17 December 2025; Received in revised form 26 February 2026; Accepted 12 April 2026

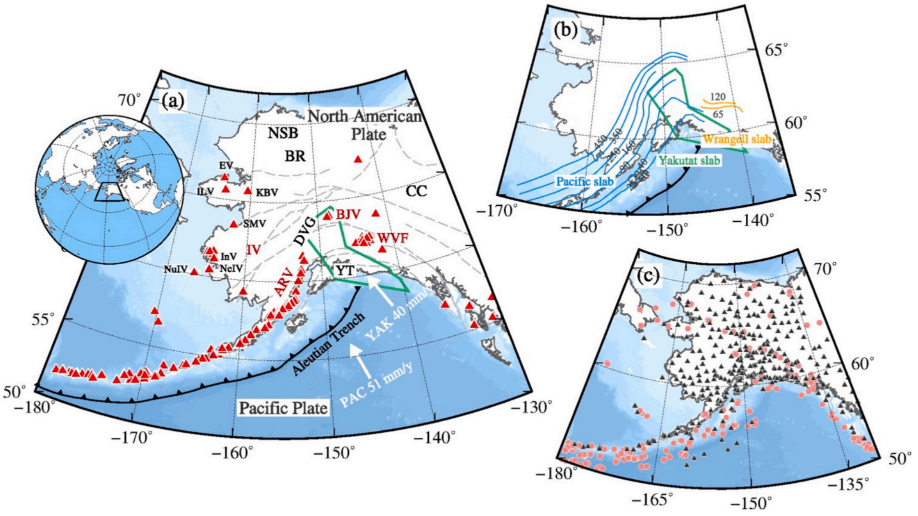

Fig. 1. (a) Regional tectonic setting. Red triangles denote the locations of volcanoes in Alaska younger than 2 million years (Cameron and Crass, 2022). The Yakutat Terrane is outlined by a green polygon (Eberhart-Phillips et al., 2006). The white vectors represent the motion velocities of the Pacific and Yakutat plates relative to North America (Elliott et al., 2010; Leonard et al., 2007). The gray dashed lines represent major fault systems (Koehler, 2013; Wilson et al., 2015). ARV: Aleutian arc volcanoes; BJV: Buzzard Creek–Jumbo Dome volcanoes; BR: Brooks Range; CC: Canadian Cordillera; DVG: Denali volcanic gap; EV: Espenberg volcano; ILV: Imuruk Lake volcano; InV: Ingakslugwat volcanoes; IV: Intraplate volcano; KBV: Koyuk-Buckland volcano; KMV: Kookooligit Mountains volcano; NeIV: Nelson Island volcano; NuIV: Nunivak Island volcano; NSB: North Slope Basin; SMV: St. Michael volcano; WVF: Wrangell volcanic field; YT: Yakutat Terrane. (b) The upper boundary isobaths of the Pacific/Yakutat and Wrangell slabs based on P-wave velocity tomographic results (Gou et al., 2019). (c) Map showing the locations of the stations (black triangles) and earthquakes (red dots) used in this study. (For interpretation of the references to colour in this figure legend, the reader is referred to the web version of this article.)

slab or small-scale slab segments may produce clustered volcanism (e.g., Jiang et al., 2018). (4) Based on a combination of numerical simulations (Jadamec and Billen, 2010) and seismic anisotropy observations (e.g., McPherson et al., 2020; Venereau et al., 2019), the magmas of the WVF were considered to have originated from melted mantle materials carried by potential toroidal mantle flow around the edge of the Yakutat slab. Given these controversies, a more detailed investigation of the lithospheric thermal structure is required to elucidate the formation of volcanism and the volcanic gap.

Cenozoic intraplate volcanoes are widespread in western Alaska and are located relatively far from the subduction trench (Fig. 1a). Unlike the volcanoes in south-central Alaska, these intraplate volcanoes have been the focus of few studies. Liang et al. (2024) proposed that slab dehydration and hot upwelling from the stagnant Pacific slab may contribute to intraplate volcanism in western Alaska, a phenomenon similar to observations in the west Pacific subduction zone (Zhao et al., 2009). However, the low-velocity anomalies beneath intraplate volcanoes are less pronounced than those beneath arc volcanoes (Liang et al., 2024). To address this, we apply a new type of observation to investigate the mantle attenuation structure beneath Alaska's intraplate volcanoes, aiming to gain a deeper understanding of their formation.

Seismic attenuation (or quality factor Q, its inverse) tomography provides valuable constraints on the anelastic structures of the lithosphere and is highly sensitive to underground temperature and partial melting (Boyd et al., 2004; Takei, 2017; Yamauchi and Takei, 2024). Several seismic attenuation studies have been conducted in this region (e.g., Hearn, 2021; Mahanama and Cramer, 2023; Mahanama et al., 2024; Soto Castaneda et al., 2021; Stachnik et al., 2004). However, detailed attenuation information in the uppermost mantle is still lacking. As the first arrival at epicentral distances between 200 and 2000 km, the seismic Pn wave primarily propagates through the uppermost mantle. It travels through the crust near the source, refracts at the Moho discontinuity, and continues along the crust to the surface. In this study, we developed a broadband Pn-wave attenuation model for the uppermost mantle beneath the Alaskan mainland using regional broadband waveform data. A two-layer attenuation model is further developed, encompassing the subcrustal lithospheric attenuation structure identified in this study and the crustal attenuation structure previously constructed from Lg-wave attenuation tomography (Yang et al., 2024). By integrating previous geological and geophysical observations, we establish links between the genesis of Alaskan volcanoes and strong crustal and uppermost-mantle attenuation anomalies, providing new insights into the formation of the DVG, WVF, and intraplate volcanism.

2. Data and methods

The regional waveform dataset comprises recordings from 253 crustal earthquakes documented by 368 permanent and temporary broadband stations in Alaska and northwestern Canada (Fig. 1c). The focal depths of these earthquakes are shallower than the Moho, as specified in the CRUST1.0 model (Laske et al., 2013). These events occurred between January 2000 and August 2021, with focal mechanisms obtained from the Harvard Centroid Moment Tensor Catalog (Ekstrom et al., 2012). The magnitudes range from 4.0 to 8.5. To ensure that Pn-wave is the first-arriving phase and can be reliably distinguished from the crustal Pg phase, we confined the epicentral distances to 200–2000 km, using only events recorded by more than three stations. The selection criterion required a minimum of three Pn records per station to ensure the station's validity and improve the robustness of the inversion. Detailed information on the stations and earthquakes is provided in Tables S1-S3 in the Supporting Information.

Fig. 2 illustrates the processing flow for calculating the spectral amplitude of Pn-waves, following the methods of Zhao et al. (2015) and Yang et al. (2023). First, we removed the mean and linear trend of raw waveforms and applied 10% cosine tapers at both ends. Then, the displacement waveforms were obtained after removing instrumental responses (Fig. 2a). We sampled the Pn signal within a 0.7 km/s-long group velocity window (Fig. 2c), extending 0.3 km/s before and 0.4 km/s after the IASP91 first arrival (red line in Fig. 2a). The waveforms were subsequently inspected manually, and only high-quality records were retained for further analysis. The noise was extracted before the first P arrival within a window of the same length as the Pn waveform (Fig. 2b). The Pn and noise spectra were obtained through fast Fourier transformation (FFT), where the spectral amplitudes were sampled at 42

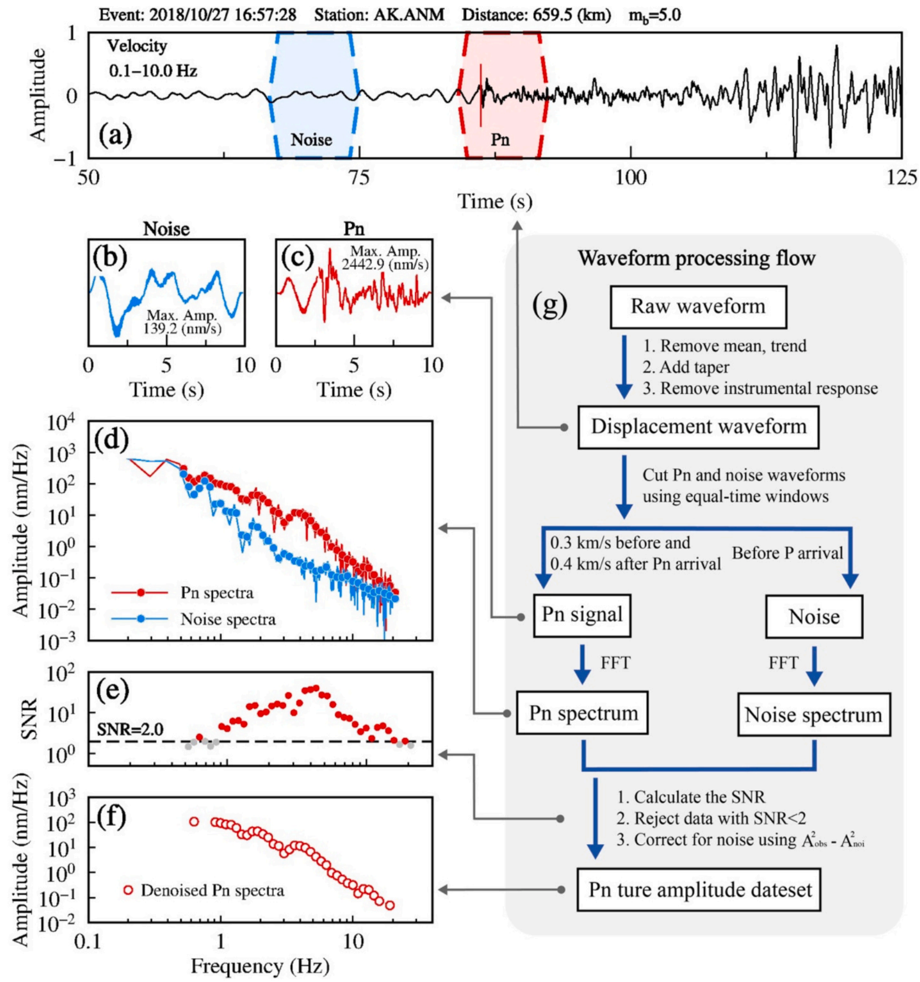

Fig. 2. Pn amplitude measurement. (a) Vertical-component seismograms from the 2018/10/27 earthquake recorded at station AK.ANM, where the noise (blue) and Pn signals (red) were sampled within two equal-time length windows. The onset of the Pn phase is marked by a vertical red line, determined based on the theoretical first-arrival times predicted by the IASP91 model and the epicentral distance. (b-c) Enlarged waveforms of the noise and Pn signal. (d) Pn and noise spectra. (e) SNR for data selection, where data with an SNR < 2.0 were removed (gray dots). (f) Denoised Pn spectra. (g) Waveform processing flow. (For interpretation of the references to colour in this figure legend, the reader is referred to the web version of this article.)

discrete frequencies evenly distributed between 0.5 and 20.0 Hz on a logarithmic scale (Fig. 2d). Note that Figs. 2b–2c show **velocity waveforms**, with units of nm/s, whereas the spectral amplitudes in Fig. 2d are derived from **displacement waveforms** (units of nm) and thus have units of nm/Hz, or equivalently nm·s. A signal-to-noise ratio (SNR) of 2.0 was employed as the threshold for data selection (Fig. 2e). In general, amplitudes at low frequencies ($f< 1.0$ Hz) or very high frequencies ($f> 10.0$ Hz) exhibit lower SNRs, consequently diminishing the available data amount and imaging resolution. The denoised Pn spectral amplitudes were derived using $A_s^2(f) = A_o^2(f) - A_n^2(f)$ (Fig. 2f), where the subscripts s, o, and n denote the clear, observed and noisy signals, respectively (Ringdal et al., 1992). At 1.0 Hz, 6368 Pn amplitudes were obtained, constituting the final imaging dataset. Two-station amplitude ratios were further calculated for pairs of stations with similar great-circle paths.

The geometric spreading of Pn-wave is relatively complex, exhibiting dependencies on both distance and frequency (e.g., Zhu et al., 1991). In this study, we employed a simulated annealing algorithm to fine-tune the geometric spreading parameters (Yang et al., 2007; Yang, 2011), aligning them with the actual amplitude data to construct the Pn-wave geometric spreading model in and around the Alaska mainland (Yang et al., 2023; Zhao et al., 2015) (see Text S1 for details). Moho depth variations in Alaska are relatively small compared with the epicentral distance range considered in this study (200–2000 km) (Miller and Moresi, 2018). Consequently, the influence of Moho topography on Pn-wave amplitudes is expected to be minor relative to geometric spreading and is unlikely to exert a first-order control.

Single-station amplitude measurements offer dense raypath coverage, while two-station amplitude ratios effectively suppress the trade-off between source effects and attenuation. The joint inversion of these two datasets, therefore, enhances both the spatial resolution and the stability of the tomographic results. In practice, the theoretical amplitude and amplitude-ratio formulations are converted into the logarithmic domain and linearized, forming a unified inversion framework for the combined dataset. To increase the number of two-station raypaths, pairs of stations with similar azimuths were approximated as lying on the same great-circle path. At each frequency, single- and two-station data were jointly inverted using the iterative least-squares orthogonal factorization (LSQR) method (Paige and Saunders, 1982). The initial Q_{Pn} model at each frequency was set as a constant value calculated by the linear fitting of amplitude ratios. During each iteration, the change in Q value (δQ) remains small, while the background Q^0 is iteratively updated until the root mean square residual of the amplitude becomes stable. Finally, we obtained the Pn Q distributions at 42 discrete frequencies, along with the source terms and site responses. Details of the tomographic methodology are provided in Text S1 of the Supporting Information.

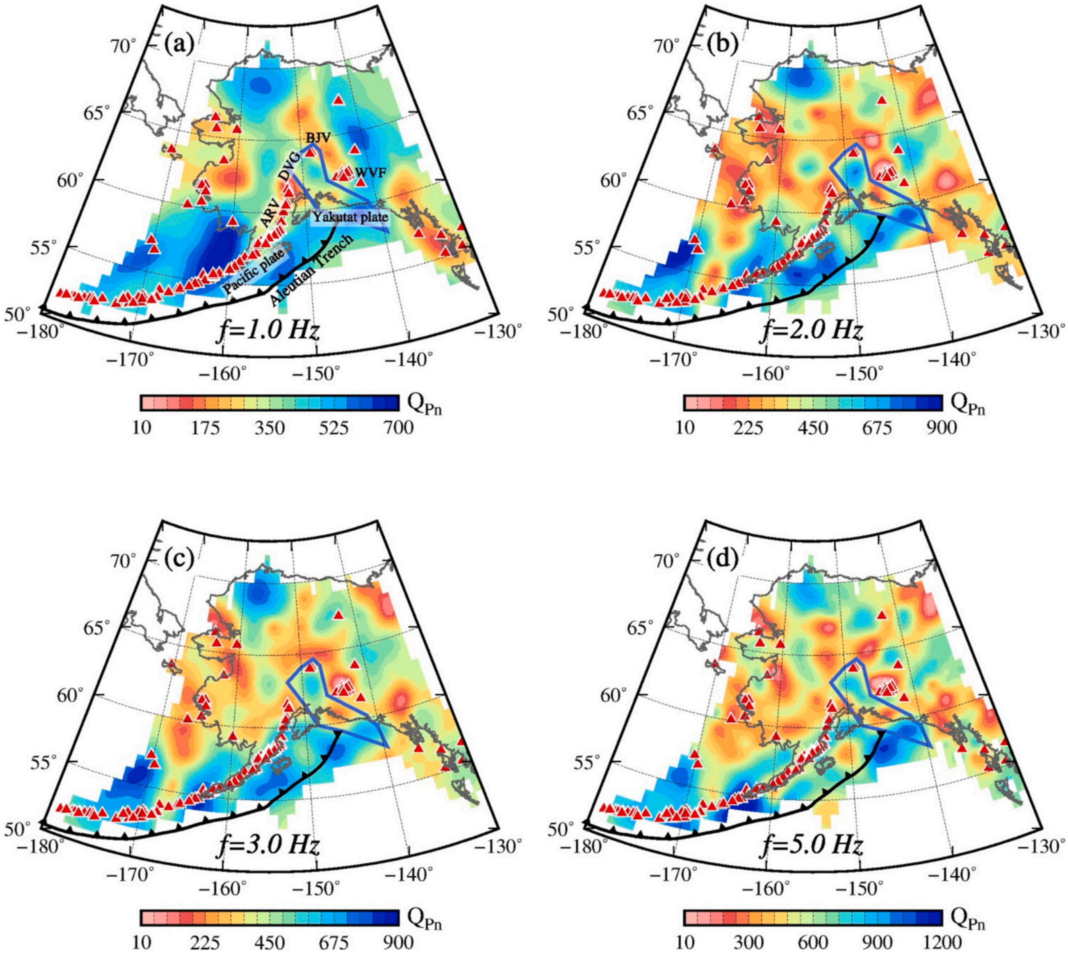

Fig. 3. Selected Q_{Pn} images at 1.0, 2.0, 3.0, and 5.0 Hz, respectively. The red triangles denote the locations of volcanoes. (For interpretation of the references to colour in this figure legend, the reader is referred to the web version of this article.)

3. Results

3.1. Broadband Pn-wave attenuation model

A high-resolution Pn-wave attenuation model was constructed for the uppermost mantle beneath the Alaskan mainland at 42 individual frequencies ranging from 0.5 to 20.0 Hz. Fig. 3 displays four selected Q_{Pn} maps at 1.0, 2.0, 3.0, and 5.0 Hz. The Pn attenuation exhibits frequency dependence. Here, we partitioned the study area into seven major geological units according to lithospheric lithology and age (Colpron et al., 2007), and calculated their attenuation frequency dependencies between 0.5 and 20.0 Hz (Fig. S1). For each unit, Q_{Pn} values were extracted from the grid nodes contained within the unit and averaged to produce representative attenuation–frequency curves. The Arctic Alaska Terrane (AAT) and the Pacific and Yakutat plates display higher Q_{Pn} values than other regions within the frequency range of 1.5–6.0 Hz. The Ocean Domain Terranes (ODT), Wrangellia Composite Terrane (WCT), and Yukon Composite Terrane (YCT) all exhibit apparent low Q_{Pn} values between 1.0 and 5.0 Hz. At frequencies exceeding 5.0 Hz or below 1.0 Hz, the Q_{Pn} curves gradually overlap and intersect. Pn signal exhibits a higher signal-to-noise ratio (SNR) between 1.0 and 5.0 Hz, allowing us to obtain more high-quality data (Fig. S2). Thus, we finally identified the 1.0–5.0 Hz frequency band as the dominant band for the Pn-wave attenuation model.

The broadband Pn-wave attenuation model was obtained by calculating the logarithmic average of Q_{Pn} values between 1.0 and 5.0 Hz (Fig. 4a). Because Pn energy can penetrate several tens of kilometers below the Moho at epicentral distances of 200–2000 km (Xie and Lay, 2017), this model represents the average attenuation structure of the uppermost mantle at corresponding depths. In northern Alaska, the uppermost mantle beneath the North Slope Basin presents distinct high-Q_{Pn} features ($Q_{Pn} > 600$). The Canadian Cordillera (CC) also exhibits weak Pn attenuation, especially at lower frequencies ($Q_{Pn} > 500$ at 1.0 Hz, Fig. 3a). In southern Alaska, high-Q_{Pn} anomalies corresponding to cold oceanic plates are identified near the subduction trench. Additionally, the shape of the high-Q_{Pn} zone closely aligns with the Yakutat plate, which has also been identified as a high-velocity feature in velocity tomography (e.g., Gou et al., 2019; Liang et al., 2024; Liu and Gao, 2025; Liu et al., 2025). The Q_{Pn} beneath the Pacific and Yakutat plates ranges from 600 to 800, whereas the Aleutian arc volcanoes (ARV), BJV, and WVF surrounding the Yakutat Terrane all exhibit strong attenuation features ($Q_{Pn} < 250$). A wide range of strong attenuation zones ($Q_{Pn} < 250$) is observed beneath the ODT in western Alaska, where numerous intraplate volcanoes have developed. Low Pn velocity anomalies were also observed beneath volcanic regions in south-central and western Alaska (He and Lü, 2021). In a previous study, we obtained a broadband crustal Lg-wave attenuation model for the Alaskan mainland using the same dataset (Fig. 4b, Yang et al., 2024). The North Slope Basin (NSB) and CC feature both high-Q_{Pn} and high-Q_{Lg} features in the uppermost mantle and crust, respectively. The strong attenuation anomalies beneath the arc and intraplate volcanic areas typically extend into the uppermost mantle and crust. Around the Yakutat plate, a toroidal high-attenuation zone is observed in the uppermost mantle and crust. The DVG exhibits high-Q_{Pn} and high-Q_{Lg} features, corresponding to the absence of surface volcanism.

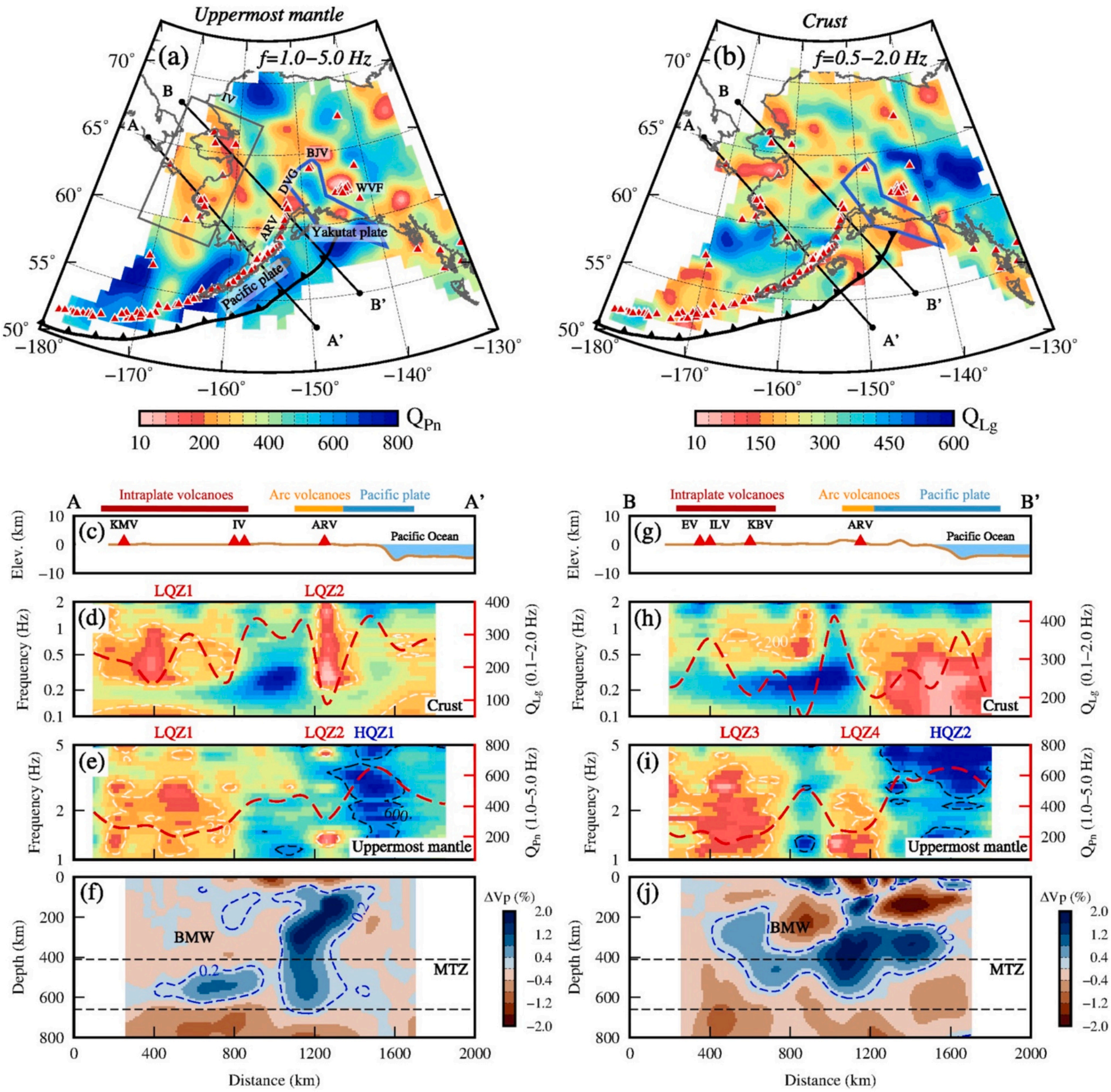

Fig. 4. Comparisons among frequency-dependent Q, seismic velocity, and volcanic activity. (a) Uppermost mantle Pn-wave attenuation model between 1.0 and 5.0 Hz. Black lines mark the locations of the profiles. The gray box indicates the region where intraplate volcanoes developed. (b) Crustal Lg-wave attenuation model between 0.5 and 2.0 Hz (Yang et al., 2024). (c-f) Profile *A-A′* showing volcanic activity and surface topography (c), Q_{Lg} (from Yang et al., 2024) versus frequency (d), Q_{Pn} versus frequency (e), and P-wave velocity perturbation (f, Liang et al., 2024) profiles. The red dashed lines represent the average Q_{Lg} and Q_{Pn} curves in panels (d) and (e). (g-j) Similar to (c-f), but for profile B-B′. Note that only profiles (e) and (i) represent new findings from this study. LQZ1–4: low-Q zones 1–4; HQZ1–2: high-Q zones 1–2; BMW: big mantle wedge; MTZ: mantle transition zone. (For interpretation of the references to colour in this figure legend, the reader is referred to the web version of this article.)

3.2. *Resolution and uncertainty tests*

We conducted a series of checkerboard resolution tests at multiple frequencies (Figs. S3–S5). In the input model, the regional average Q_{Pn} was used as the background, with attenuation anomalies introduced as ±20% perturbations. Synthetic amplitudes were generated using the same station and event distributions, based on known source terms and a geometric-spreading model derived from the inversion of real data. The signal-to-noise ratio (SNR) of the amplitudes ranges from approximately 5 to 40 (Fig. 2e), corresponding to noise levels of 20% to 2.5%. Due to uncertainties in the geometric spreading model, source functions, and site responses, the actual noise level may be higher. To assess this effect, checkerboard resolution tests were performed with 5%, 20%, and 40% random noise added. The results indicate that the resolution reaches $1^\circ \times 1^\circ$ with 5% and 20% noise (Figs. S3–S4) and $1.5^\circ \times 1.5^\circ$ with 40% noise (Fig. S5). Adding random noise leads to unreliable recovery in areas with sparse raypath coverage. Therefore, the effective resolution of our Q_{Pn} model is between $1^\circ \times 1^\circ$ and $1.5^\circ \times 1.5^\circ$.

The uncertainty in Q_{Pn} was examined using the bootstrapping technique (Efron, 1983). We reconstructed the attenuation model 100 times, randomly selecting 80% of the ray paths from the entire single- and two-station datasets. The mean Q_{Pn} map closely resembles the directly inverted Q_{pn} map (Fig. S6). At most nodes, the standard deviations are significantly smaller than the mean values, confirming the robustness of the data quality control and inversion system.

4. Discussion

4.1. Comparison with velocity models

Multiple studies have investigated the lithospheric velocity structure of the Alaskan mainland using various seismic imaging techniques, including surface wave tomography (e.g., Feng and Ritzwoller, 2019; Liu et al., 2022; Wang and Tape, 2014), body wave tomography (e.g., Gou et al., 2019; He and Lü, 2021; Liang et al., 2024; Martin-Short et al., 2016; Qi et al., 2007), joint inversion of multiple datasets (e.g., Berg et al., 2020; Jiang et al., 2018; Liu et al., 2025; Martin-Short et al., 2018), and full-wave tomography (e.g., Liu and Gao, 2025; Yang and Gao, 2020). Our Pn-wave attenuation model represents the average attenuation structure of the uppermost mantle several tens of kilometers below the Moho but lacks depth resolution. Consequently, it cannot be directly compared with velocity slices at specific depths. Here, we selected velocity maps at representative depths for comparison (Fig. S7). In the upper mantle, the first-order features of our attenuation model are broadly consistent with previous velocity models. For instance, high-velocity and high-Q_{Pn} anomalies occur in the Brooks Range in the north, the CC in the northeast, and near the Aleutian trench, whereas low-velocity and low-Q_{Pn} regions are concentrated in south-central Alaska (Berg et al., 2020; Feng and Ritzwoller, 2019). Nevertheless, some differences also exist between attenuation and velocity models. Previous velocity tomographic studies have identified the high-velocity Yakutat plate in the upper mantle at depths of ~80–150 km (e.g., Gou et al., 2019; Liang et al., 2024; Liu and Gao, 2025; Liu et al., 2025). However, at shallower depths corresponding to the uppermost mantle (~50 km), some velocity models do not clearly resolve the shape of the Yakutat plate. In contrast, our Pn-wave attenuation model shows a high-Q_{Pn} anomaly that aligns well with the boundaries of the Yakutat plate in this depth range. Beneath western Alaska, we identified new low-Q_{Pn} anomalies beneath intraplate volcanoes, in contrast to the sporadic low-velocity anomalies in the same region. Furthermore, discrepancies exist among different velocity models, such as the inconsistent distribution of low- and high-velocity features east of the Yakutat slab. Studies focusing specifically on Pn velocity imaging remain relatively limited (He and Lü, 2021). In south-central Alaska, He and Lü (2021) reported a high Pn velocity anomaly associated with the Yakutat plate, which aligns well with our wedge-shaped high-Q_{Pn} anomaly. Although low Pn velocity anomalies were also detected around the Yakutat plate, they appear less continuous than the toroidal low-Q_{Pn} belt revealed in this study. In western Alaska, low Pn velocity anomalies are observed beneath the intraplate volcanoes, corresponding well with low-Q_{Pn} features. However, the amplitudes of the low-velocity anomalies are relatively small. These discrepancies are reasonable given differences in data coverage and methodology.

4.2. Strong attenuation beneath the intraplate volcanoes

Many intraplate volcanoes have developed in western Alaska and the Bering Sea, located at considerable distances from the Aleutian trench (Fig. 1a). Fig. 4 shows two Q-frequency profiles, *A-A′* and *B-B′*, across the Aleutian trench, ARV, and intraplate volcanoes. The low-Q_{Pn} anomalies are stable across a wide frequency band beneath both arc and intraplate volcanoes (Fig. 4e and i), consistent with high heat flow (>90 mW/m^2) beneath ARV, WVF, and intraplate volcanic regions (Batir et al., 2016). These observations suggest that the strong attenuation anomalies in the uppermost mantle are related to elevated temperatures. The subducting Pacific plate exhibits weak attenuation ($Q_{Pn} > 600$) in the uppermost mantle. Low Q_{Lg} values in the crust correspond well with low Q_{Pn} values beneath intraplate and arc volcanoes (Fig. 4d and h). Two local minima and a local maximum are correlated with volcanic regions and the subducting plate in the broadband Q_{Lg} and Q_{Pn} curves. This pattern is more clearly expressed in profile *A-A′*. We suggest that hot magmatic material may exist in the uppermost mantle and further intrude into the crust, leading to intraplate volcanic activity in western Alaska. Although only a few stations deployed in the Bering Sea were used, the raypath coverage and resolution tests (Fig. S3) indicate that the attenuation feature along the western edge of Alaska is robust. The presence of peridotite xenoliths in intraplate volcanic rocks further supports an origin from backarc mantle magmatism (Moll-Stalcup, 1994).

The subduction pattern of the North Pacific plate remains controversial, making it difficult to explain the deep magmatic origins of the intraplate volcanoes in western Alaska. Numerous seismic velocity tomography studies have imaged the high-velocity Pacific slab subducting to depths of 300–500 km; however, they cannot effectively explain the origins of these intraplate volcanoes (Gou et al., 2019; Jiang et al., 2018; Martin-Short et al., 2016; Qi et al., 2007). Liang et al. (2024) conducted P-wave velocity tomography and identified a flat, high-velocity anomaly in the mantle transition zone (MTZ) at depths of 410–670 km. They suggested that a “big mantle wedge” (BMW) structure has formed beneath western Alaska, similar to the conditions observed in the west Pacific (Zhao et al., 2009). Some low-velocity anomalies are observed beneath the intraplate volcanoes, although they are less pronounced than those beneath the arc volcanoes (Fig. 4f and j). In our attenuation model, extensive low-Q_{Pn} and low-Q_{Lg} anomalies are observed in the crust and uppermost mantle beneath the intraplate volcanoes. These anomalies are situated above the flat slab at depths of 410–670 km, as observed by velocity tomography. Both the attenuation and velocity images support the notion that intraplate volcanoes may be fed by hot, wet upwellings from the BMW (Liang et al., 2024).

Interestingly, the low-Q_{Pn} anomalies in western Alaska are distributed in two NW–SE-trending belts (Fig. 4a), suggesting the presence of two hot upwellings that may feed the two volcanic groups (group 1: EV, ILV, KBV, and SMV; group 2: KMV, InV, NuIV, and NeIV). The two low-Q_{Pn} belts are oriented approximately parallel to the subduction direction, extending over ~500 km, and are also observed in non-volcanic regions. Their spatial extent aligns well with the length of the stagnant Pacific slab in the MTZ (Fig. 4). We therefore propose that the intraplate volcanism in western Alaska is closely linked to the dynamics of the stagnant Pacific slab. Because the cold Pacific plate subducts rapidly, dehydration reactions may be incomplete in the shallower upper mantle. The stagnant slab may undergo continuous dehydration, inducing sustained hot upwelling along the subduction direction (Poli and Schmidt, 2002; Zhao et al., 2009). These hot materials ascend into the upper mantle, forming the observed intraplate volcanoes and associated low-Q_{Pn} anomalies. Low-velocity and high electrical conductivity features in the MTZ (e.g., Conder and Wiens, 2006; Zhao et al., 2009), petrological and mineralogical experiments (Huang et al., 2005; Komabayashi et al., 2004; Shieh et al., 1998), and numerical simulations (Iwamori, 2004; Richard et al., 2006) support the possible dehydration of the stagnant Pacific slab. However, the direct relationship between seismic attenuation and melt presence remains controversial (Abers et al., 2014; Holtzman, 2016; Takei, 2017; Yamauchi and Takei, 2024). Mineral physics studies have shown that subsolidus effects, physical processes occurring at temperatures below the solidus, can also produce high seismic attenuation near magma source regions without the presence of melt (Takei, 2017, and references therein). This implies that seismic imaging may detect low-Q regions that are larger than the actual molten zones. In this study, we suggest that the two low-Q_{Pn} belts correspond to high-temperature zones in the uppermost mantle. These high temperature anomalies may reflect melting, but further quantitative constraints are required to confirm this interpretation.

Global- and regional-scale tomographic models have revealed a stagnant Pacific slab beneath northeastern Asia (Zhao et al., 2009). The intraplate volcanic rocks in the western Pacific are also characterized by alkalic basalts and minor tholeiitic basalts, which contain peridotite xenoliths (Liu et al., 2001). This BMW structure and intraplate volcanism are comparable to those in western Alaska. Fig. S8 presents a Pn-wave attenuation model (1.0–15.0 Hz) for the Sea of Japan and

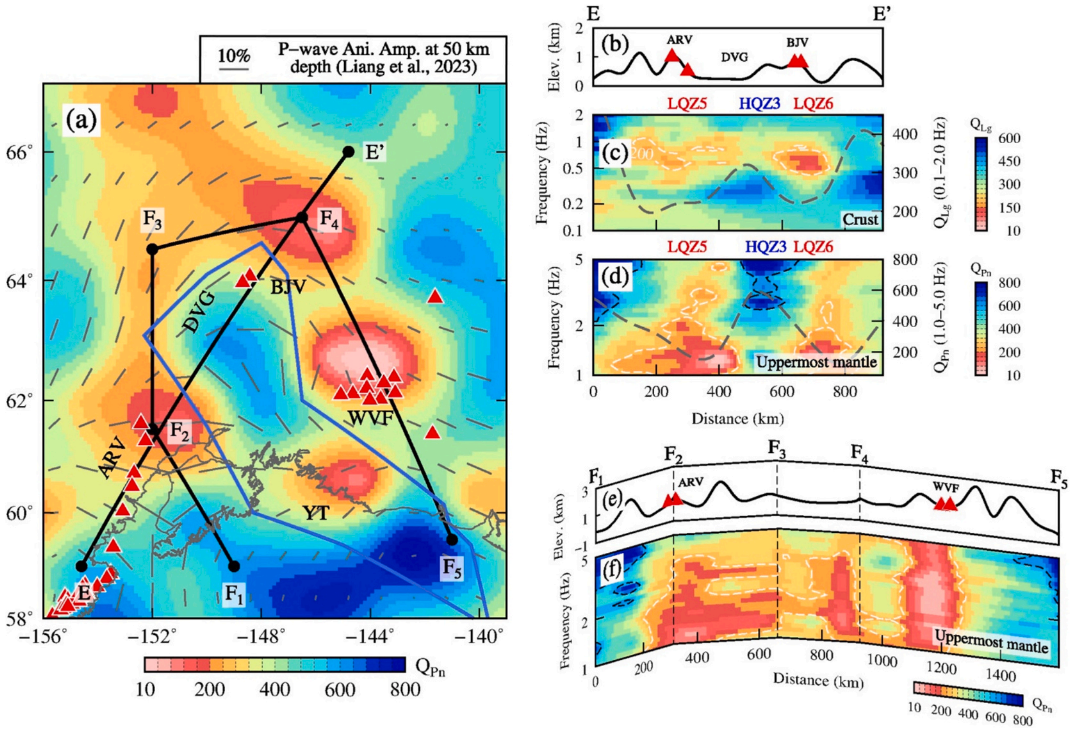

Fig. 5. Toroidal low-Q_{Pn} attenuation features around the Yakutat Terrane. (a) Broadband Pn-wave attenuation map in south-central Alaska. Two selected profiles are marked in black. The gray lines denote P-wave 3-D fast velocity directions (FVDs) projected on a horizontal plane; the line length denotes the anisotropic amplitude, and the scale is shown in the top-right (Liang et al., 2024). (b-d) Profile *E–E′* showing volcanic activity and surface topography (b), Q_{Lg} versus frequency (c), and Q_{Pn} versus frequency (d) profiles. The gray dashed lines represent the average Q_{Lg} (0.1–2.0 Hz) and Q_{Pn} (1.0–5.0 Hz) curves. LQZ5–6: low-Q zones 5–6, HQZ3: high-Q zone 3. (e-f) Profile $F_1 - F_5$ showing volcanic activity and surface topography (e) and Q_{Pn} versus frequency (f) profiles.

adjacent areas (Yang et al., 2022). Two distinct low-Q_{Pn} anomalies are observed beneath the Changbaishan (CV) and Jingpohu volcanoes (JV) (Fig. S8b). The low-Q_{Pn} anomalies beneath the Japanese arc volcanoes (JRV) are situated adjacent to the high-Q_{Pn} Pacific slab. The Q_{Pn} variation exhibits consistent features from the subduction trench to the backarc region in both the western and northeastern Pacific subduction zones. The intraplate volcanoes in both the western Pacific and Alaska may originate from mantle upwelling associated with BMW dynamics.

4.3. *Toroidal melting around the Yakutat Plate*

The DVG spans ~400 km between the ARV and the BJV (Fig. 5a). The *Q*-frequency profile *E–E′* reveals two low-Q_{Pn} and low-Q_{Lg} anomalies beneath the ARV and BJV (Figs. 5c-5d). Near the BJV, the crustal low-Q_{Lg} anomaly is located directly beneath the BJV, while the low-Q_{Pn} anomaly in the uppermost mantle is slightly offset to the northeast of the volcanic centers. We suggest that the formation of the BJV is associated with this nearby low-Q_{Pn} anomaly in the uppermost mantle, implying that the hot material may upwell with a minor lateral deviation rather than following a strictly vertical path. The DVG exhibits weak Pn- and Lg-wave attenuations, indicating that large amounts of magmatic material are unlikely to be present in the uppermost mantle and crust. The shape of the high-Q_{Pn} anomaly beneath the DVG aligns well with the subducted Yakutat slab. Compared with the Pacific plate, the high-Q_{Pn} Yakutat plate extends farther in the subduction direction (northwest) in the uppermost mantle and features a lower subduction angle. Consequently, the top of the Yakutat slab is trapped in the uppermost mantle due to the low subduction angle, and the cold mantle wedge beneath the DVG cannot generate sufficient melt to sustain surface volcanism. Similar volcanic absences and nonvolcanic tremors have been observed in other warm subduction zones around the Pacific, such as Cascadia and southwestern Japan (Delph et al., 2018; Obara, 2002). Chuang et al. (2017) suggested that most fluids are expelled at shallower depths near the tremor zone, thereby preventing the generation of significant partial melts at depth that would feed arc volcanism. This pattern aligns with the weak attenuation features observed in the crust and uppermost mantle beneath the DVG. The WVF is situated on the eastern side of the Yakutat terrane, where the major volcanoes consist of large andesitic shield volcanoes and large volumes of calc-alkaline volcanic rocks (Preece and Hart, 2004; Richter et al., 1990). In the uppermost mantle and crust, the WVF is associated with a clustered strong attenuation anomaly and has lower Q_{Lg} and Q_{Pn} values than the ARV and the BJV (Figs. 5a and 4b). In profile $F_1 - F_5$, the stable low-Q_{Pn} anomaly persists across a wide frequency band (Fig. 5f). These observations indicate that hot mantle upwelling may contribute to the formation of the WVF.

The flat subduction of the Yakutat microplate induced distinctive anisotropic features in south-central Alaska. Shear-wave splitting analysis has revealed a rotational fast direction around the edge of the Yakutat slab (Venereau et al., 2019). Rotational P- and S-wave fast-velocity directions also suggest toroidal mantle flow around the slab edge (Feng et al., 2020; Gou et al., 2019; Liang et al., 2024). In the uppermost mantle, low-Q_{Pn} anomalies are not limited to those beneath volcanoes. We observe a toroidal low-Q_{Pn} zone around the Yakutat terrane, which corresponds well with the rotational fast-velocity directions (Fig. 5a). Furthermore, a toroidal melting zone with low Q_{Lg} values has also been observed in the crust (Fig. 4b, Yang et al., 2024). To test the resolvability of such an attenuation pattern, a synthetic test was conducted (Fig. S9). The results show that the inversion system can effectively distinguish the high-Q_{Pn} Yakutat plate from the toroidal low-Q_{Pn} zone. We further designed a synthetic test model with three spatially isolated low-Q_{Pn} anomalies and performed inversion (Fig. S10). Although minor smearing occurs, it does not generate the fully connected pattern seen in Fig. S9. These results support the interpretation that the flat subduction of the Yakutat microplate likely induces toroidal mantle flow.

The origin of the WVF remains debated, with several mechanisms

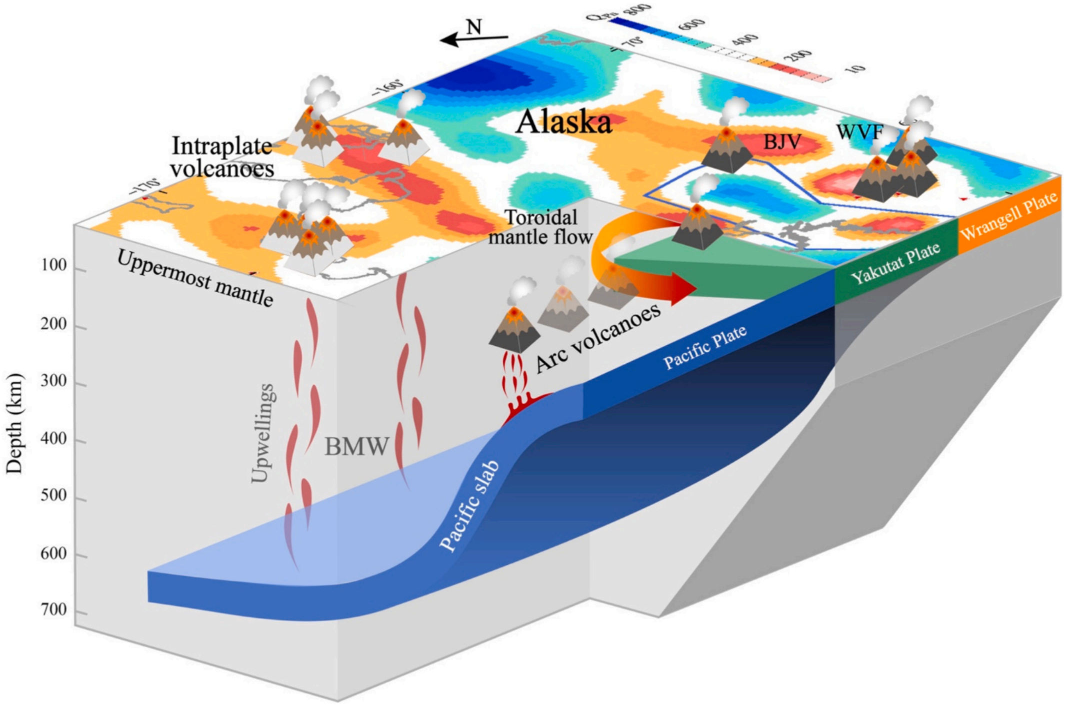

Fig. 6. Schematic diagram illustrating the origin of volcanism in Alaska. The subduction patterns of the Pacific (blue), Yakutat (green), and Wrangell (orange) slabs are constrained by seismic velocity tomography (Gou et al., 2019; Liang et al., 2024). BMW: big mantle wedge. (For interpretation of the references to colour in this figure legend, the reader is referred to the web version of this article.)

proposed. One hypothesis suggests that partial melting at the edge of the Yakutat slab generates adakitic magmas, which may account for Wrangell volcanism (Preece and Hart, 2004). Alternatively, a slab gap or tear could provide a pathway for magma ascent (Gou et al., 2019; Mann et al., 2022). The subduction of the Wrangell slab or smaller slab fragments has also been proposed to focus volcanic activity (e.g., Boyce et al., 2023; Jiang et al., 2018; Yang and Gao, 2020). Finally, toroidal mantle flow around the Yakutat slab may facilitate mantle upwelling beneath the WVF (e.g., Venereau et al., 2019). Our attenuation observations do not clearly distinguish between the slab gap model and the mantle upwelling model associated with the Yakutat slab. However, given the presence of a toroidal low-Q zone surrounding the Yakutat plate, we favor the interpretation that the hot, partially molten material carried by the toroidal mantle flow feeds the WVF and the BJV, creating a toroidal melting zone in the uppermost mantle and crust.

5. Conclusion

Our high-resolution Q_{Pn} maps delineate potential high-temperature zones in the uppermost mantle beneath both intraplate and arc volcanoes (Fig. 6). Low-Q_{Pn} anomalies beneath western Alaska reveal two primary belt-like high temperature zones associated with the intraplate volcanoes. Given the clear spatial correspondence between these strong attenuation anomalies and the stagnant Pacific slab, the formation of intraplate volcanism in Alaska is likely associated with the BMW structure. Combined with crustal attenuation variations (Yang et al., 2024), the weak attenuation features beneath the DVG suggest that the flat subduction of the Yakutat slab has created cold mantle and crustal environments, inhibiting the generation of partial melts and leading to the absence of volcanism. In contrast, the ARV and BJV, adjacent to the DVG, exhibit significantly low-Q_{Pn} and low-Q_{Lg} anomalies. The strong attenuation anomalies observed throughout the crust and uppermost mantle provide evidence for hot upwelling beneath the WVF. Around the Yakutat plate, partially molten materials transported by toroidal mantle flow may supply the WVF and the BJV, generating a toroidal melting zone in the uppermost mantle and crust that manifests as a circular high-attenuation feature.

CRediT authorship contribution statement

Geng Yang: Writing – original draft, Visualization, Validation, Software, Resources, Methodology, Investigation, Formal analysis, Data curation, Conceptualization. **Lian-Feng Zhao:** Writing – review & editing, Supervision, Software, Project administration, Methodology, Funding acquisition, Data curation, Conceptualization. **Xiao-Bi Xie:** Writing – review & editing, Supervision, Methodology, Conceptualization. **Yingjie Yang:** Writing – review & editing, Supervision, Project administration, Funding acquisition, Conceptualization. **Zhen-Xing Yao:** Supervision, Funding acquisition.

Declaration of competing interest

The authors have no conflicts of interest to disclose.

Acknowledgments

The comments from Editor G. Houseman and two anonymous reviewers are valuable and greatly improved this manuscript. This research was supported by the National Natural Science Foundation of China (42430306 and 42404067), the Postdoctoral Fellowship Program of CPSF (GZC20240638), and the China Postdoctoral Science Foundation (2024M751295 and 2025T180104). We thank Xuran Liang for providing the P-wave velocity model for comparison (Liang et al., 2024). Certain figures were generated using Generic Mapping Tools (https://www.generic-mapping-tools.org).

Appendix A. Supplementary data

Supplementary data to this article can be found online at https://doi.org/10.1016/j.tecto.2026.231206.

Data availability

The waveforms used in this study were collected from the Incorporated Research Institutions for EarthScope Data Management Center. Detailed station information and corresponding references are provided in Table S2 of the Supporting Information. The single- and two-station Pn amplitude data used in this study and the resulting Pn-wave attenuation model are publicly available at doi:10.12197/2024GA028.

References

Abers, G.A., Fischer, K.M., Hirth, G., Wiens, D.A., Plank, T., Holtzman, B.K., McCarthy, C., Gazel, E., 2014. Reconciling mantle attenuation-temperature relationships from seismology, petrology, and laboratory measurements. Geochem. Geophys. Geosyst. 15, 3521–3542. https://doi.org/10.1002/2014gc005444.

Batir, J.F., Blackwell, D.D., Richards, M.C., 2016. Heat flow and temperature-depth curves throughout Alaska: finding regions for future geothermal exploration. J. Geophys. Eng. 13, 366–378. https://doi.org/10.1088/1742-2132/13/3/366.

Berg, E.M., Lin, F.C., Allam, A., Schulte-Pelkum, V., Ward, K.M., Shen, W., 2020. Shear velocity model of Alaska via joint inversion of rayleigh wave ellipticity, phase velocities, and receiver functions across the Alaska transportable array. J. Geophys. Res. Solid Earth 125. https://doi.org/10.1029/2019jb018582.

Boyce, A., Liddell, M.V., Pugh, S., Brown, J., McMurchie, E., Parsons, A., Estève, C., Burdick, S., Darbyshire, F.A., Cottaar, S., Bastow, I.D., Schaeffer, A.J., Audet, P., Schutt, D.L., Aster, R.C., 2023. A new p-wave tomographic model (CAP22) for north america: Implications for the subduction and cratonic metasomatic modification history of western Canada and Alaska. J. Geophys. Res. Solid Earth 128. https://doi.org/10.1029/2022jb025745.

Boyd, O.S., Jones, C.H., Sheehan, A.F., 2004. Foundering lithosphere imaged beneath the southern Sierra Nevada, California, USA. Science 305, 660–662. https://doi.org/10.1126/science.1099181.

Cameron, C.E., Crass, S.W., 2022. Geologic Database of Information on Volcanoes in Alaska (GeoDIVA): Alaska Division of Geological & Geophysical Surveys Digital Data Series, p. 20. https://doi.org/10.14509/30901.

Christeson, G.L., Gulick, S.P., van Avendonk, H.J., Worthington, L.L., Reece, R.S., Pavlis, T.L., 2010. The Yakutat terrane: dramatic change in crustal thickness across the transition fault, Alaska. Geology 38, 895–898. https://doi.org/10.1130/G31170.1.

Chuang, L., Bostock, M., Wech, A., Plourde, A., 2017. Plateau subduction, intraslab seismicity, and the denali (Alaska) volcanic gap. Geology 45, 647–650. https://doi.org/10.1130/g38867.1.

Colpron, M., Nelson, J.L., Murphy, D.C., 2007. Northern cordilleran terranes and their interactions through time. GSA Today 17. https://doi.org/10.1130/gsat01704-5a.1.

Conder, J.A., Wiens, D.A., 2006. Seismic structure beneath the Tonga arc and lau backarc basin determined from joint vp, Vp/Vs tomography. Geochem. Geophys. Geosyst. 7. https://doi.org/10.1029/2005gc001113.

Delph, J.R., Levander, A., Niu, F., 2018. Fluid controls on the heterogeneous seismic characteristics of the cascadia margin. Geophys. Res. Lett. 45. https://doi.org/10.1029/2018gl079518.

Eberhart-Phillips, D., Christensen, D.H., Brocher, T.M., Hansen, R., Ruppert, N.A., Haeussler, P.J., Abers, G.A., 2006. Imaging the transition from aleutian subduction to Yakutat collision in Central Alaska, with local earthquakes and active source data. J. Geophys. Res. Solid Earth 111. https://doi.org/10.1029/2005jb004240.

Efron, B., 1983. Estimating the error rate of a prediction rule: improvement on cross-validation. J. Am. Stat. Assoc. 78, 316–331. https://doi.org/10.1080/01621459.1983.10477973.

Ekstrom, G., Nettles, M., Dziewonski, A.M., 2012. The global CMT project 2004-2010: Centroid-moment tensors for 13,017 earthquakes. Phys. Earth Planet. In. 200, 1–9. https://doi.org/10.1016/j.pepi.2012.04.002.

Elliott, J.L., Larsen, C.F., Freymueller, J.T., Motyka, R.J., 2010. Tectonic block motion and glacial isostatic adjustment in Southeast Alaska and adjacent Canada constrained by GPS measurements. Journal of Geophysical Research-Solid Earth. 115. https://doi.org/10.1029/2009jb007139.

Feng, L., Ritzwoller, M.H., 2019. A 3-D shear velocity model of the crust and uppermost mantle beneath Alaska including apparent radial anisotropy. J. Geophys. Res. Solid Earth 125, e2020JB020076. https://doi.org/10.1029/2020JB020076.

Feng, L., Liu, C., Ritzwoller, M.H., 2020. Azimuthal anisotropy of the crust and uppermost mantle beneath Alaska. J. Geophys. Res. Solid Earth 125. https://doi.org/10.1029/2020jb020076.

Gou, T., Zhao, D., Huang, Z., Wang, L., 2019. Aseismic deep slab and mantle flow beneath Alaska: Insight from anisotropic tomography. J. Geophys. Res. Solid Earth 124, 1700–1724. https://doi.org/10.1029/2018jb016639.

He, Y., Lü, Y., 2021. Anisotropic pn tomography of Alaska and adjacent regions. J. Geophys. Res. Solid Earth 126. https://doi.org/10.1029/2021jb022220.

Hearn, T.M., 2021. Crustal attenuation from USArray ML amplitude tomography. Geophys. J. Int. 224, 199–206. https://doi.org/10.1093/gji/ggaa445.

Holtzman, B.K., 2016. Questions on the existence, persistence, and mechanical effects of a very small melt fraction in the asthenosphere. Geochem. Geophys. Geosyst. 17, 470–484. https://doi.org/10.1002/2015gc006102.

Huang, X.G., Xu, Y.S., Karato, S.I., 2005. Water content in the transition zone from electrical conductivity of wadsleyite and ringwoodite. Nature 434, 746–749. https://doi.org/10.1038/nature03426.

Iwamori, H., 2004. Phase relations of peridotites under H₂O-saturated conditions and ability of subducting plates for transportation of H₂O. Earth Planet. Sci. Lett. 227, 57–71. https://doi.org/10.1016/j.epsl.2004.08.013.

Jadamec, M.A., Billen, M.I., 2010. Reconciling surface plate motions with rapid three-dimensional mantle flow around a slab edge. Nature 465, 338–341. https://doi.org/10.1038/nature09053.

Jiang, C., Schmandt, B., Ward, K.M., Lin, F.C., Worthington, L.L., 2018. Upper mantle seismic structure of Alaska from rayleigh and s wave tomography. Geophys. Res. Lett. 45. https://doi.org/10.1029/2018gl079406.

Koehler, R.D., 2013. Quaternary Faults and Folds (QFF): Alaska Division of Geological & Geophysical Surveys Digital Data Series 3. https://doi.org/10.14509/24956.

Komabayashi, T., Omori, S., Maruyama, S., 2004. Petrogenetic grid in the system MgO-SiO₂-H₂O up to 30 GPa, 1600°C:: applications to hydrous peridotite subducting into the Earth's deep interior -: art. no. B03206. J. Geophys. Res. Solid Earth 109. https://doi.org/10.1029/2003jb002651.

Laske, G., Masters, G., Ma, Z., Pasyanos, M., 2013. Update on CRUST1.0 – A 1-degree global model of Earth's crust, EGU General Assembly 2013, Vienna, Austria.

Leonard, L.J., Hyndman, R.D., Mazzotti, S., Nykolaishen, L., Schmidt, M., Hippchen, S., 2007. Current deformation in the northern Canadian cordillera inferred from GPS measurements. Journal of Geophysical Research-Solid Earth. 112. https://doi.org/10.1029/2007jb005061.

Liang, X., Zhao, D., Hua, Y., Xu, Y.G., 2024. Big mantle wedge and intraplate volcanism in Alaska: Insight from anisotropic tomography. J. Geophys. Res. Solid Earth 129. https://doi.org/10.1029/2023jb027617.

Liu, C., Zhang, S., Sheehan, A.F., Ritzwoller, M.H., 2022. Surface wave isotropic and azimuthally anisotropic dispersion across Alaska and the Alaska-Aleutian subduction zone. J. Geophys. Res. Solid Earth 127. https://doi.org/10.1029/2022jb024885.

Liu, J., Han, J., Fyfe, W.S., 2001. Cenozoic episodic volcanism and continental rifting in northeast China and possible link to Japan Sea development as revealed from K–Ar geochronology. Tectonophysics 339, 385–401. https://doi.org/10.1016/S0040-1951(01)00132-9.

Liu, M., Gao, H., 2025. Controls of slab subduction and tearing on the magmatism of Wrangell volcanoes in south-Central Alaska. Geophys. Res. Lett. 52. https://doi.org/10.1029/2024gl113139.

Liu, Z., Liang, C., Cao, F., Fan, X., Chen, C., 2025. Mechanisms for layered anisotropy and anomalous magmatism of Alaska subduction system revealed by ambient noise tomography and the wave gradiometry method. J. Geophys. Res. Solid Earth 130. https://doi.org/10.1029/2024jb029105.

Mahanama, A., Cramer, C.H., 2023. Lateral variations of attenuation in the crust of Alaska using lg q tomography. Bull. Seismol. Soc. Am. 113, 1054–1063. https://doi.org/10.1785/0120220164.

Mahanama, A., Gabrielli, S., Cramer, C.H., Akinci, A., 2024. Separation of intrinsic and scattering seismic wave attenuation in the crust of central and south-Central Alaska. Bull. Seismol. Soc. Am. 114, 2963–2977. https://doi.org/10.1785/0120240094.

Mann, M.E., Abers, G.A., Daly, K.A., Christensen, D.H., 2022. Subduction of an oceanic plateau across southcentral Alaska: scattered-wave imaging. J. Geophys. Res. Solid Earth 127. https://doi.org/10.1029/2021jb022697.

Martin-Short, R., Allen, R.M., Bastow, I.D., 2016. Subduction geometry beneath south Central Alaska and its relationship to volcanism. Geophys. Res. Lett. 43, 9509–9517. https://doi.org/10.1002/2016gl070580.

Martin-Short, R., Allen, R., Bastow, I.D., Porritt, R.W., Miller, M.S., 2018. Seismic imaging of the Alaska subduction zone: Implications for slab geometry and volcanism. Geochem. Geophys. Geosyst. 19, 4541–4560. https://doi.org/10.1029/2018gc007962.

McPherson, A.M., Christensen, D.H., Abers, G.A., Tape, C., 2020. Shear wave splitting and mantle flow beneath Alaska. J. Geophys. Res. Solid Earth 125. https://doi.org/10.1029/2019jb018329.

Miller, M.S., Moresi, L., 2018. Mapping the alaskan moho. Seismol. Res. Lett. 89, 2430–2436. https://doi.org/10.1785/0220180222.

Moll-Stalcup, E.J., 1994. Latest cretaceous and cenozoic magmatism in mainland Alaska. In: Plafker, G., Berg, H.C. (Eds.), The geology of Alaska. Geological Society of America, pp. 589–618.

Obara, K., 2002. Nonvolcanic deep tremor associated with subduction in Southwest Japan. Science 296, 1679–1681. https://doi.org/10.1126/science.1070378.

Paige, C.C., Saunders, M.A., 1982. LSQR: an algorithm for sparse linear equations and sparse least squares. ACM Trans. Math. Softw. 8, 43–71.

Plafker, G., Moore, J.C., Winkler, G.R., 1994. Geology of the Southern Alaska Margin. Geology of the Southern Alaska Margin.

Poli, S., Schmidt, M.W., 2002. Petrology of subducted slabs. Annu. Rev. Earth Planet. Sci. 30, 207–235. https://doi.org/10.1146/annurev.earth.30.091201.140550.

Preece, S.J., Hart, W.K., 2004. Geochemical variations in the <5 ma Wrangell volcanic field, Alaska: Implications for the magmatic and tectonic development of a complex continental arc system. Tectonophysics 392, 165–191. https://doi.org/10.1016/j.tecto.2004.04.011.

Qi, C., Zhao, D., Chen, Y., 2007. Search for deep slab segments under Alaska. Phys. Earth Planet. In. 165, 68–82. https://doi.org/10.1016/j.pepi.2007.08.004.

Rabade, S., Lin, F.C., Tape, C., Ward, K.M., Waldien, T., Allam, A., 2023. The crustal magmatic structure beneath the denali volcanic gap imaged by a dense linear seismic array. J. Geophys. Res. Solid Earth 128. https://doi.org/10.1029/2023jb027152.

Richard, G., Bercovici, D., Karato, S.I., 2006. Slab dehydration in the earth's mantle transition zone. Earth Planet. Sci. Lett. 251, 156–167. https://doi.org/10.1016/j.epsl.2006.09.006.

Richter, D.H., Smith, J.G., Lanphere, M.A., Dalrymple, G.B., Reed, B.L., Shew, N., 1990. Age and progression of volcanism, Wrangell volcanic field, Alaska. Bull. Volcanol. 53, 29–44.

Ringdal, F., Marshall, P.D., Alewine, R.W., 1992. Seismic yield determination of soviet underground nuclear explosions at the shagan river test site. Geophys. J. Int. 109, 65–77. https://doi.org/10.1111/j.1365-246X.1992.tb00079.x.

Shieh, S.R., Mao, H.K., Hemley, R.J., Ming, L.C., 1998. Decomposition of phase d in the lower mantle and the fate of dense hydrous silicates in subducting slabs. Earth Planet. Sci. Lett. 159, 13–23. https://doi.org/10.1016/s0012-821x(98)00062-4.

Soto Castaneda, R.A., Abers, G.A., Eilon, Z.C., Christensen, D.H., 2021. Teleseismic attenuation, temperature, and melt of the upper mantle in the Alaska subduction zone. J. Geophys. Res. Solid Earth 126. https://doi.org/10.1029/2021jb021653.

Stachnik, J.C., Abers, G.A., Christensen, D.H., 2004. Seismic attenuation and mantle wedge temperatures in the Alaska subduction zone. J. Geophys. Res. Solid Earth 109. https://doi.org/10.1029/2004jb003018.

Takei, Y., 2017. Effects of Partial Melting on Seismic Velocity and Attenuation: A New Insight from experiments. In: Jeanloz, R., Freeman, K.H. (Eds.), Annual Review of Earth and Planetary Sciences, vol. 45, pp. 447–470.

Venereau, C.M.A., Martin-Short, R., Bastow, I.D., Allen, R.M., Kounoudis, R., 2019. The role of variable slab dip in driving mantle flow at the eastern edge of the alaskan subduction margin: Insights from shear-wave splitting. Geochem. Geophys. Geosyst. https://doi.org/10.1029/2018gc008170.

Wang, Y., Tape, C., 2014. Seismic velocity structure and anisotropy of the Alaska subduction zone based on surface wave tomography. J. Geophys. Res. Solid Earth 119, 8845–8865. https://doi.org/10.1002/2014jb011438.

Ward, K.M., Lin, F.C., 2018. Lithospheric structure across the alaskan cordillera from the joint inversion of surface waves and receiver functions. J. Geophys. Res. Solid Earth 123, 8780–8797. https://doi.org/10.1029/2018jb015967.

Wilson, F.H., Hults, C.P., Mull, C.G., Karl, S.M., 2015. Geologic Map of Alaska: U.S. Geological Survey Scientific Investigations Map 3340. pamphlet 196 p., 2 sheets, scale 1:1,584,000. https://doi.org/10.3133/sim3340.

Xie, X.B., Lay, T., 2017. Frequency-Dependent effects of 2D random velocity heterogeneities in the mantle lid onPnGeometric spreading. Bull. Seismol. Soc. Am. 107, 482–488. https://doi.org/10.1785/0120160186.

Yamauchi, H., Takei, Y., 2024. Effect of melt on polycrystal anelasticity. J. Geophys. Res. Solid Earth 129. https://doi.org/10.1029/2023jb027738.

Yang, G., Zhao, L.F., Xie, X.B., He, X., Lü, Y., Yao, Z.X., 2022. “Double door” opening of the Japan Sea inferred by pn attenuation tomography. Geophys. Res. Lett. 49. https://doi.org/10.1029/2022gl099886.

Yang, G., Chen, L., Zhao, L.F., Xie, X.B., Yao, Z.X., 2023. Segmented Up-Bending of the arabian continental plate revealed by Pn attenuation tomography. J. Geophys. Res. Solid Earth 128. https://doi.org/10.1029/2023jb028062.

Yang, G., Zhao, L.F., Xie, X.B., He, X., Zhang, L., Yao, Z.X., 2024. Strong lg-wave attenuation reveals quarter-toroidal crustal melting around the Yakutat terrane in south-Central Alaska. J. Geophys. Res. Solid Earth 129. https://doi.org/10.1029/2024jb029104.

Yang, X., Gao, H., 2020. Segmentation of the Aleutian-Alaska subduction zone revealed by full-wave ambient noise tomography: implications for the along-strike variation of volcanism. J. Geophys. Res. Solid Earth 125. https://doi.org/10.1029/2020jb019677.

Yang, X., Lay, T., Xie, X.B., Thorne, M.S., 2007. Geometric spreading of pn and sn in a spherical earth model. Bull. Seismol. Soc. Am. 97, 2053–2065. https://doi.org/10.1785/0120070031.

Yang, X.N., 2011. A pn spreading model constrained with observed amplitudes in asia. Bull. Seismol. Soc. Am. 101, 2201–2211. https://doi.org/10.1785/0120100314.

Zhao, D., Tian, Y., Lei, J., Liu, L., Zheng, S., 2009. Seismic image and origin of the changbai intraplate volcano in east asia: Role of big mantle wedge above the stagnant pacific slab. Phys. Earth Planet. In. 173, 197–206. https://doi.org/10.1016/j.pepi.2008.11.009.

Zhao, L.F., Xie, X.B., Tian, B.F., Chen, Q.F., Hao, T.Y., Yao, Z.X., 2015. Pn wave geometrical spreading and attenuation in Northeast China and the korean peninsula constrained by observations from north korean nuclear explosions. J. Geophys. Res. Solid Earth 120, 7558–7571. https://doi.org/10.1002/2015jb012205.

Zhu, T.F., Chun, K.Y., West, G.F., 1991. Geometrical spreading and q of pn waves: an investigative study in eastern Canada. Bull. Seismol. Soc. Am. 81, 882–896.